Theoretical Investigation of Relaxation Dynamics in $Au_{38}(SH)_{24}$ Thiolate-Protected Gold Nanocluster

Ravithree D. Senanayake [†], Emilie B. Guidez [‡], Amanda J. Neukirch [§], Oleg V. Prezhdo [¥] and Christine M. Aikens [†]*

[†]Department of Chemistry, Kansas State University, Manhattan, KS 66506, USA

[‡]Department of Chemistry, University of Colorado Denver, Denver, CO 80217-3364, USA

[§]Theoretical Division, Los Alamos National Laboratory, Los Alamos, NM 87545, USA

[¥]Department of Chemistry, University of Southern California, Los Angeles, CA 90089-1062, USA

* cmaikens@ksu.edu, 1-785-532-0954, fax: 1-785-532-6666

Abstract

A subtle change in the electronic structure of thiolate-protected noble metal nanoparticles can result in distinctive energy relaxation dynamics. Corresponding investigations on different sizes and structures of thiolate-protected gold nanoclusters reveal their physical and chemical properties for further development of catalytic applications. In this work, we performed nonradiative relaxation dynamics simulations of the $Au_{38}(SH)_{24}$ nanocluster to describe electron-vibrational energy exchange. The core and higher excited states involving semiring motifs lying in the energy range of 0.00-2.01 eV are investigated using time-dependent density functional theory (TDDFT). The surface hopping method with decoherence correction combined with real-time TDDFT is used to assess the quantum dynamics. The Au_{23} core relaxations are found to occur in the range of 2.0 – 8.2 ps. The higher excited states that consist of core-semiring mixed or semiring states give ultra-fast decay time constants in the range of 0.6 – 4.9 ps. Our calculations predict that the slowest individual state decay of S_{11} or the slowest combined S_{11}-S_{12}, S_1-S_2-S_6-S_7 and S_4-S_5-S_9-S_{10} decay involves intracore relaxations. The analysis of the phonon spectral densities and the ground state vibrational frequencies suggest that the low frequency (25 cm^{-1}) coherent phonon emission reported experimentally could be the

bending of the bi-icosahedral Au_{23} core or the "fan blade twisting" mode of two icosahedral units.

Introduction

Advances in synthesis and isolation of thiolate-protected gold nanoparticles have led to developments in applications such as catalysis and photocatalysis.[1-6] Investigations of energy relaxation dynamics for different sizes and structures of thiolate-protected gold nanoclusters are needed to enable elucidation of the physical and chemical properties underlying these applications.[7-13] Quantum confinement effects become prominent for small gold nanoparticles less than 2 nm in diameter. Thus, the geometric structure of the system plays a role in its electronic structure,[14-16] and subtle changes in structure can lead to different electron dynamics.[14, 17-18]

Extensive experimental work has examined the electron relaxation dynamics of nanoclusters such as $[Au_{25}(SR)_{18}]^{-1}$, and distinct time scales and relaxation mechanisms have been reported.[19-22] Recent theoretical electron-nuclear relaxation studies on the $[Au_{25}(SH)_{18}]^{-1}$ nanocluster provided insights into the experimentally proposed relaxation mechanisms.[23-24] The study by Senanayake et al. showed that states arising from orbitals based on the semirings (i.e. the –SR–Au–SR– units surrounding the nanoparticle core) or other states are not observed at an energy lower than the core-based S_1 state. Moreover, it suggested that the experimentally observed time constants in the several picoseconds range could arise from core-to-core transitions rather than from a core-to-semiring transition. Recently, Jin and co-workers reported an ultrafast relaxation dynamics of $Au_{38}(SC_2H_4Ph)_{24}$ nanoclusters and the effects of structural isomerism.[25] This study found a correlation between the ultrafast relaxation dynamics and the geometric structures of two isomers of thiolate-protected $Au_{38}(SC_2H_4Ph)_{24}$. In another study, Knappenberger and co-workers reported low-frequency vibrations associated with the ligand shell of $Au_{25}(SC_8H_9)_{18}$ and $Au_{38}(SC_{12}H_{25})_{24}$ nanoclusters that mediate the nonradiative relaxation dynamics.[26] The reported modes include Au(I)-S stretching (200 cm^{-1}) and Au(0)−Au(I) stretching (90 cm^{-1}) of the ligand shell.[26]

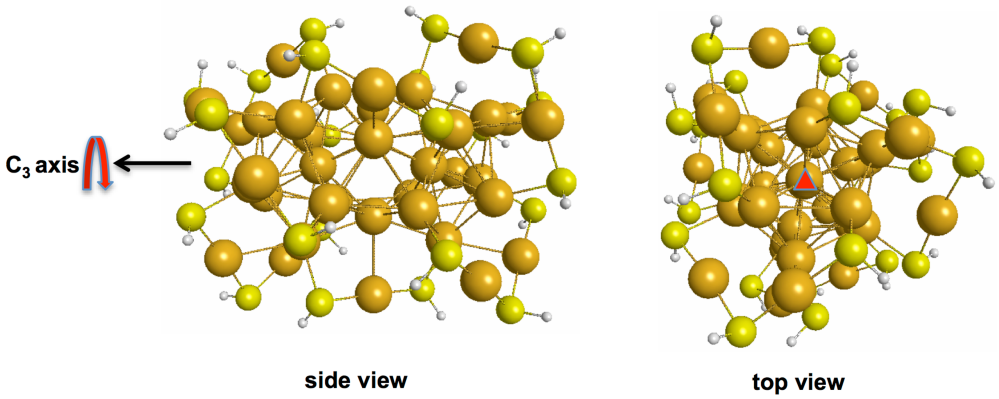

Figure 1. Geometry of the $Au_{38}(SH)_{24}$ nanocluster: side view and top view. (Au-gold, S-yellow, H-white)

The $Au_{38}(SR)_{24}$ nanocluster contains a face-fused bi-icosahedral Au_{23} core protected by six -SR-Au-SR-Au-SR- dimeric semirings and three -SR-Au-SR- monomeric semirings, forming a core-shell-like structure (Figure 1).[27-29] This nanocluster has attracted significant research interest in the areas of chirality, doping and catalysis.[26, 30-34] In 2010, Aikens and co-workers[28] showed that the arrangement of the semirings around the core yields an essentially D_3–symmetric isomer for $Au_{38}(SR)_{24}$ compared to a higher energy C_{3h} isomer. The electronic structure of the D_3 isomer can be explained based on a particle-in-a-cylinder (PIC) model due to its nanorod-shaped gold core structure.[28] Thus, the occupied and unoccupied orbitals near the HOMO-LUMO gap can be described by Σ, Π, Δ symmetries. The orbitals can be labeled as M_l, where the azimuthal quantum number M = 0, 1, 2, ... corresponds to Σ, Π, Δ, ... orbitals and l = 1, 2, 3, ... corresponds to the axial quantum number.[28] The core-shell structure of the $Au_{38}(SR)_{24}$ nanocluster can result in interesting optical properties, but careful assignment of core and ligand contributions in optical properties is important. An ultrafast luminescence investigation proposed that the electron dynamics of $Au_{38}(SR)_{24}$ includes core-to-shell relaxations.[25] However, a recent theoretical investigation on the luminescence origin of $Au_{38}(SR)_{24}$ suggested that the two lowest energy fluorescence bands arise predominantly due to a HOMO → LUMO transition that involves core-based orbitals.[35]

The experimental examination of ultrafast relaxation dynamics performed on the $Au_{38}(SC_2H_4Ph)_{24}$ nanocluster suggests that the isomer with a bi-icosahedral Au_{23} inner core shows rapid decay (1.5 ps) among excited states followed by nanosecond relaxation to the ground state, and that a higher energy structural isomer exhibits similar relaxation processes.[25] They performed the femtosecond experiments on the $Au_{38}(SR)_{24}$ isomer pumped at 490 nm/1050 nm and probed in the visible range (0.0 - 2.3 eV). They proposed a two-state relaxation model[25] similar to a mechanism proposed for the $[Au_{25}(SR)_{18}]^{-1}$. [8, 21] The picosecond relaxations in both isomers were assigned to core–shell charge transfer or to electronic rearrangement within the metal core;[25] they suggested that the picosecond decay in $Au_{38}(SR)_{24}$ could be an electronic rearrangement within the metal core based on previous experimental and theoretical work on other thiolate-protected gold clusters.[11-12, 36] For the $Au_{38}(SR)_{24}$ isomer with a bi-icosahedral core, they also reported a coherent phonon emission at 25 cm^{-1} with pumping in the near IR region.[25]

Overall, further experimental and theoretical work is required to fully understand the nonradiative relaxation dynamics of the $Au_{38}(SR)_{24}$ nanocluster. Herein, the focus of this theoretical study is to reveal the electron−nuclear dynamics and give insights into the relaxation mechanism of the thiolate-protected $Au_{38}(SR)_{24}$ nanoparticle. In this study, we use the lowest energy *D_3* isomer of the $Au_{38}(SH)_{24}$ nanocluster for the relaxation dynamics calculations.

Computational methodology

We have performed ab initio real-time nonadiabatic molecular dynamics (NA-MD) simulations to study the nonadiabatic dynamics in the $Au_{38}(SH)_{24}$ nanocluster. The fewest switches surface hopping (FSSH)[37] algorithm with the classical path approximation and a time-dependent Kohn−Sham description of electronic states (FSSH-TDKS)[38] was used in our calculations. The reported geometrical and electronic structural changes (~0.05 Å) in the $Au_{38}(SH)_{24}$ nanocluster core[35] is less than the reported geometrical and electronic structural changes (~0.33 Å) in the $[Au_{25}(SR)_{18}]^{-1}$ nanocluster upon photoexcitation.[36] Therefore, the classical path approximation in the NA-MD calculation approach is expected to be suitable to describe the nonradiative relaxation

dynamics of the $Au_{38}(SH)_{24}$ nanocluster. The decoherence-induced surface hopping (DISH)[39] scheme is utilized to include decoherence effects. The FSSH simulations in this work are performed using the PYXAID program.[40-41]

The methodology used here is similar to our previous work on $[Au_{25}(SR)_{18}]^{-1}$.[24] The $Au_{38}(SH)_{24}$ nanocluster geometry optimization is performed at the PBE[42]/TZP (frozen core) level of theory in the Amsterdam Density Functional (ADF)[43] software package to obtain the relaxed geometry at 0K. The PBE/TZP level of theory was used to keep the calculations consistent with our previous investigation on $[Au_{25}(SR)_{18}]^{-1}$.[24] The zero-order regular approximation (ZORA)[44] is used to treat scalar relativistic effects in gold. Linear response time-dependent density functional theory (TDDFT) calculations were performed using the same level of theory to compute the electronic excitations and the relevant absorption spectrum of $Au_{38}(SR)_{24}$. Absorption spectra were convoluted with Gaussian functions with full width at half-maximum values of 0.2 eV and 40 nm for the spectra plotted in eV and nm respectively. A ground state vibrational frequency calculation was performed using ADF at the same level of theory to obtain the vibrational modes of the cluster. The ADF GUI was used to plot the orbitals.

The 0K system was thermalized through a temperature ramping calculation performed at 300K. After the temperature ramping, molecular dynamics (MD) simulations were performed through density functional theory (DFT) calculations in the Vienna Ab initio Simulation Package (VASP).[45] We used projector-augmented wave pseudopotentials,[46] a kinetic energy cutoff value of 402.0 eV for the temperature ramping calculation and a 301.8 eV energy cutoff value for the MD and NA coupling calculations, a 24 Å simulation box size, gamma points, and the PBE functional in all of our VASP calculations. A MD trajectory of 5 ps in length was computed with a 1 fs integration time step. The nonadiabatic coupling elements were calculated following the same approach we used for the $[Au_{25}(SH)_{18}]^{-1}$ system.[24]

The FSSH calculations employ 3.5 ps length sub-trajectories starting from 10 different initial geometries. For each NA-MD trajectory, 1000 realizations of the stochastic FSSH/DISH state hopping trajectories were considered. We used 100 realizations of the stochastic FSSH/DISH state hopping trajectories for the largest calculation with ninety-eight excited states to reduce the computational cost.

The important electronic excited states contributing to the optical absorption spectrum of $Au_{38}(SH)_{24}$ in the energy range of 0.00−2.01 eV (visible range) were analyzed. The excited state population decay times and the ground state population increase times were calculated for the $Au_{38}(SH)_{24}$ nanocluster using the same equations and procedure mentioned in our previous study.[24] The phonon spectral density plots were drawn with a resolution of 4.8 cm^{-1}.

Results and discussion

The experimental optical absorption spectrum for the $Au_{38}(SR)_{24}$ nanocluster displays low energy peaks that lie around 0.9, 1.2, 1.7 and 2.0 eV.[47] The $Au_{38}(SH)_{24}$ spectrum calculated at the PBE level of theory gives similar peaks at 0.99, 1.26, 1.74 and 2.01 eV as shown in Figure 2, in good agreement with the experimental spectrum from Ref. 47. The calculated spectral peak positions are also in agreement with the PBE/DZ frozen core optical absorption spectrum of the lowest energy D_3 isomer by Aikens and co-workers.[28]

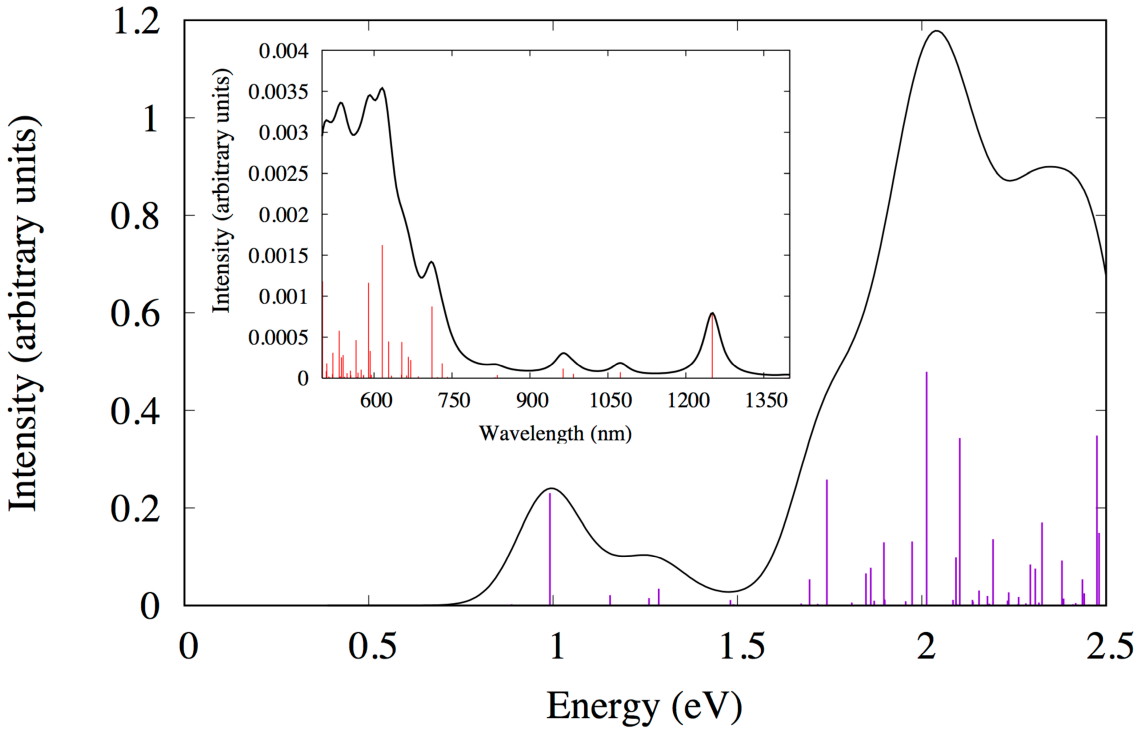

Figure 2. Calculated PBE/TZP optical absorption spectrum for $Au_{38}(SH)_{24}$. Inset: The absorption spectrum in wavelength (nm).

Relaxation dynamics of the excited state peaks up to ~ 1.5 eV

The electronic relaxations for the excitations covering the peaks up to approximately 1.5 eV will be analyzed in this section. The calculated orbitals of the $Au_{38}(SH)_{24}$ cluster near the HOMO-LUMO gap (Figure 3) can be described using Σ, Π, and Δ symmetries according to the PIC model. In $Au_{38}(SH)_{24}$, the HOMO-4 to LUMO+4 orbitals arise primarily from gold *sp* atomic orbitals in the bi-icosahedral core (Figure 3). HOMO-5 arises from 3*p* orbitals on the S atoms and 5*d* orbitals on the Au atoms in the semiring motifs. The atomic orbital contributions to the Kohn-Sham orbitals were determined from the orbital coefficients after the DFT energy calculation was performed. The orbital character found in this study is similar to the orbitals shown in the previous work by Aikens and co-workers.[28]

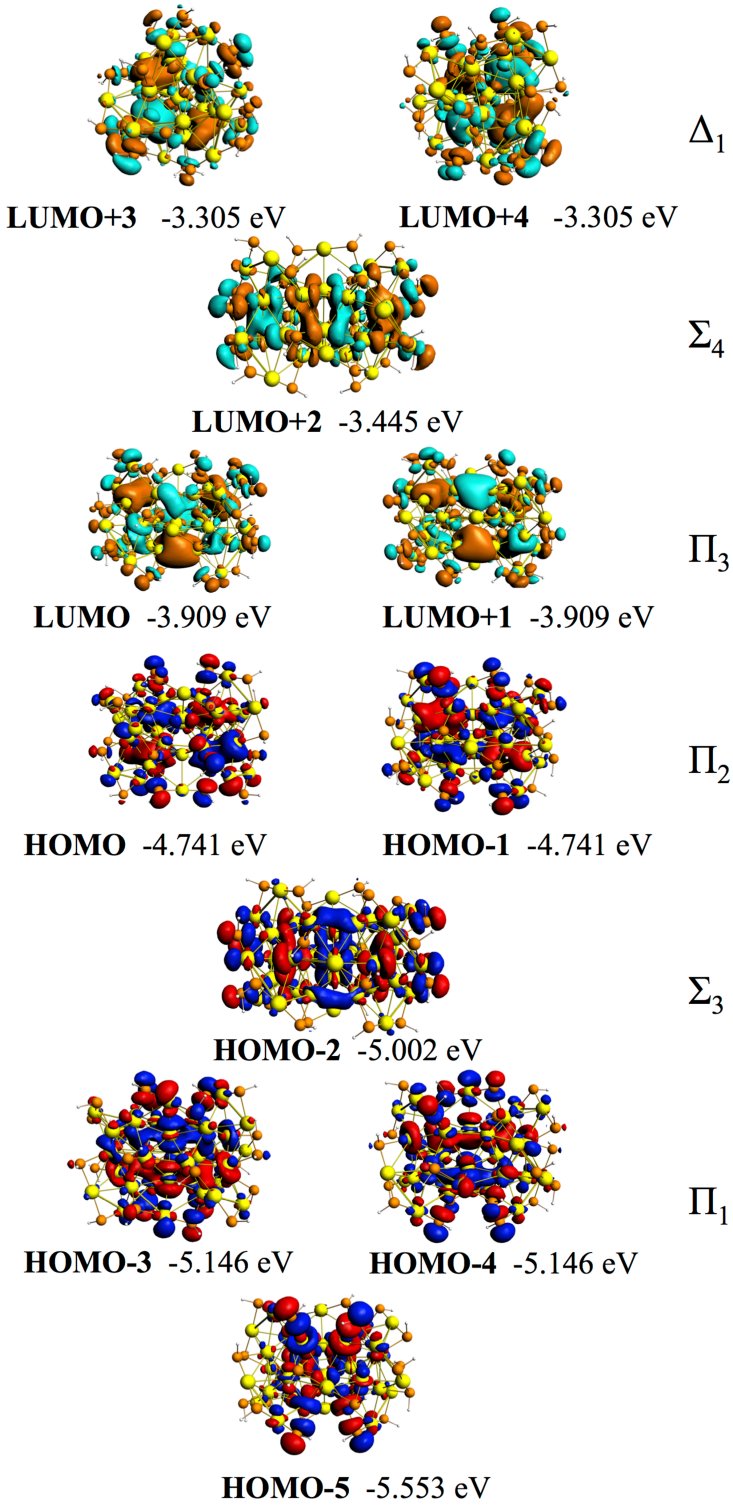

Figure 3. PBE/TZP orbitals near the HOMO−LUMO gap and their relative energies (in eV) for $Au_{38}(SH)_{24}$.

The first peak (0.99 eV) arises primarily due to a $\Pi_2 \rightarrow \Pi_3$ transition that has the highest oscillator strength and weight (Table 1), in agreement with previous results.[28] In Figure 3, the degenerate orbitals are labeled as two different orbitals. For example, HOMO and HOMO-1 are exactly degenerate in the 0 K PBE/TZP optimized structure, but become nondegenerate as the nanocluster vibrates and distorts from its equilibrium structure during the NA-MD calculations. The labeling leads to two excited states that originate primarily from HOMO and HOMO-1 to LUMO and LUMO+1 for the 0.99 eV peak in Table 1. This labeling was used in order to define the excited states that will be used in the FSSH-TDKS calculations.

Table 1 gives the excitations up to 1.5 eV with the highest oscillator strengths and weights and their respective transitions with the highest weights for the two allowed excited state symmetries A_2 and E for $Au_{38}(SH)_{24}$ (these are the dipole-allowed excited state symmetries as they contain the totally symmetric representation upon taking direct products with the dipole moment operator). The most significant transitions responsible for a particular excitation were identified based on their weights, which are all above 0.9 for the lowest energy excited states of $Au_{38}(SH)_{24}$. The excitations around 1.15-1.29 eV primarily arise from transitions out of the HOMO-2 to LUMO/LUMO+1 ($\Sigma_3 \rightarrow \Pi_3$) and transitions out of HOMO-3/HOMO-4 to LUMO/LUMO+1 ($\Pi_1 \rightarrow \Pi_3$). However, for the 1.29 eV peak the $\Sigma_3 \rightarrow \Pi_3$ transition has a small contribution to the oscillator strength and the $\Pi_1 \rightarrow \Pi_3$ transitions have higher contributions to the oscillator strength due to their higher weights. The $\Pi_1 \rightarrow \Pi_3$ transition would be a forbidden transition for a perfectly cylindrical system. Similar observations have been made by Aikens and co-workers.[28] We find that HOMO-4 to LUMO+4 orbitals are involved in the highest weighted transitions in excited states up to the 1.5 eV range (Table 1). Therefore, the twenty-five states defined for the FSSH-TDKS calculations cover this range. The excited states defined in Table 2 represent a single Slater determinant, whereas the TDDFT excitations listed in Table 1 are mixed (i.e., linear combinations of several Slater determinants); the Slater determinants defined in Table 2 include the Slater determinants present in the TDDFT calculations.

Table 1. Transitions with the highest weights for the excited states covering up to 1.5 eV from the TDDFT calculation.

Excited State	Energy (eV)	Oscillator strength	Weight	Most weighted transitions
E symmetry				
1	0.89	0.0006	0.9927	HOMO/HOMO-1 → LUMO/LUMO+1
2	1.15	0.0045	0.9381	HOMO-2 → LUMO/LUMO+1
			0.0452	HOMO-3/HOMO-4 → LUMO/LUMO+1
3	1.29	0.0074	0.9348	HOMO-3/HOMO-4 → LUMO/LUMO+1
			0.0389	HOMO-2 → LUMO/LUMO+1
4	1.33	0.0001	0.9888	HOMO/HOMO-1 → LUMO+2
5	1.49	0.0006	0.9602	HOMO/HOMO-1 → LUMO+3/LUMO+4
A_2 symmetry				
1	0.99	0.0491	0.934	HOMO/HOMO-1 → LUMO/LUMO+1
			0.0427	HOMO-2 → LUMO+2
2	1.26	0.0033	0.9749	HOMO-3/HOMO-4 → LUMO/LUMO+1
			0.0097	HOMO-2 → LUMO+2
3	1.48	0.0024	0.9729	HOMO/HOMO-1 → LUMO+3/LUMO+4
			0.0085	HOMO-2 → LUMO+2

Table 2. Excited states, corresponding transitions (covering 0.00-1.50 eV energy range) used in the FSSH-TDKS calculations, and their average energies during the MD simulation.

Excited state	Transitions	Average energy of the excited state (eV)
S_1	HOMO → LUMO	0.70
S_2	HOMO → LUMO+1	0.81
S_3	HOMO → LUMO+2	0.99
S_4	HOMO → LUMO+3	1.14
S_5	HOMO → LUMO+4	1.29
S_6	HOMO-1 → LUMO	0.83
S_7	HOMO-1 → LUMO+1	0.95
S_8	HOMO-1 → LUMO+2	1.13
S_9	HOMO-1 → LUMO+3	1.27
S_{10}	HOMO-1 → LUMO+4	1.43
S_{11}	HOMO-2 → LUMO	1.09
S_{12}	HOMO-2 → LUMO+1	1.21
S_{13}	HOMO-2 → LUMO+2	1.38
S_{14}	HOMO-2 → LUMO+3	1.53
S_{15}	HOMO-2 → LUMO+4	1.68

S_{16}	HOMO-3 → LUMO	1.19
S_{17}	HOMO-3 → LUMO+1	1.30
S_{18}	HOMO-3 → LUMO+2	1.48
S_{19}	HOMO-3 → LUMO+3	1.63
S_{20}	HOMO-3 → LUMO+4	1.78
S_{21}	HOMO-4 → LUMO	1.27
S_{22}	HOMO-4 → LUMO+1	1.38
S_{23}	HOMO-4 → LUMO+2	1.56
S_{24}	HOMO-4 → LUMO+3	1.71
S_{25}	HOMO-4 → LUMO+4	1.86

Figure 4 demonstrates the variation of the orbital energies with time for the $Au_{38}(SH)_{24}$ cluster as obtained from the MD simulations. The orbital energy variation shows the near-degenerate nature of several sets of the orbitals. For example, the HOMO and HOMO-1 as well as the LUMO and LUMO+1 are nearly degenerate. As mentioned above, the degeneracies of the orbitals shown in Figure 3 were obtained by performing a single point calculation on the relaxed geometry at 0K. However, the MD simulation was performed at 300K. During the dynamics, the $Au_{38}(SH)_{24}$ cluster geometry can have distortions in the *x*, *y* and *z* directions that break the perfect D_3 symmetry of the optimized $Au_{38}(SH)_{24}$ geometry. During the MD simulation, the HOMO-LUMO gap of the $Au_{38}(SH)_{24}$ cluster is approximately 0.70 eV (Figure 4), which is smaller than the 0.83 eV gap obtained at 0K.

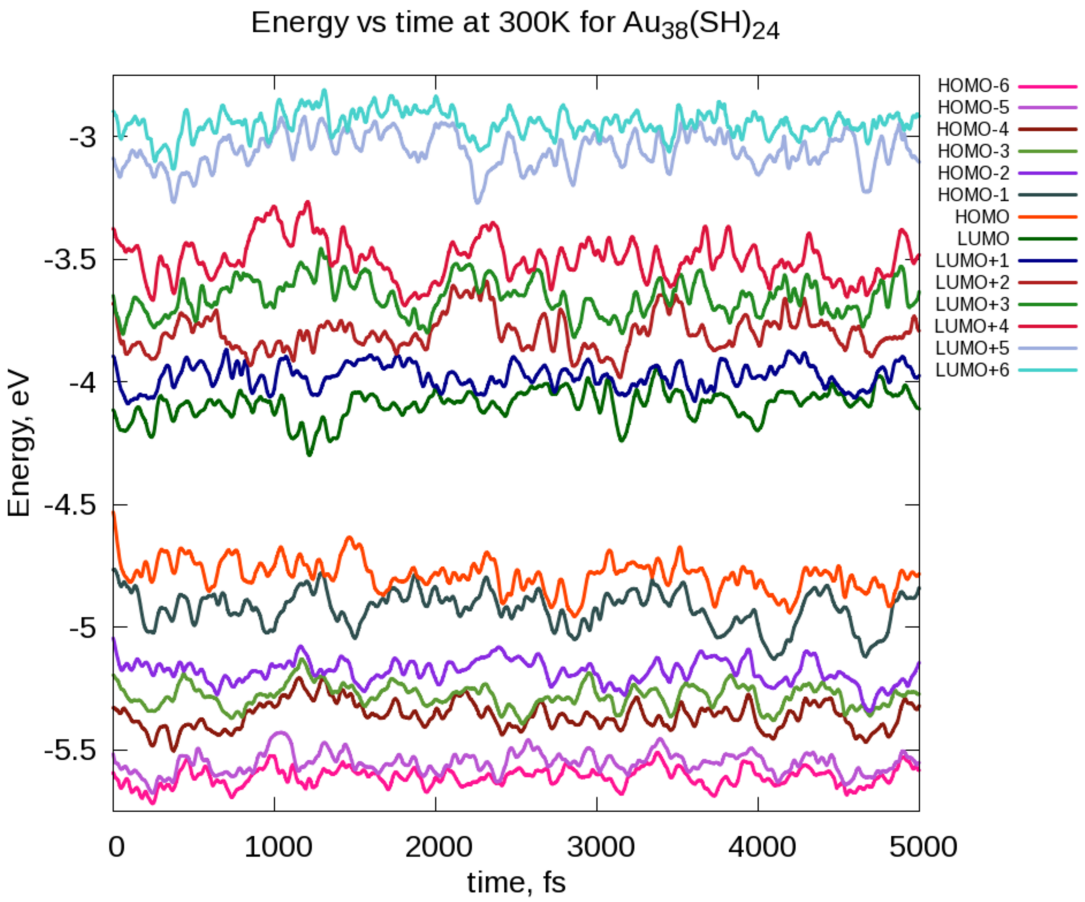

Figure 4. Variation of the HOMO−6 to LUMO+6 orbital energies with time.

Relaxation dynamics of the first peak ~ 1.5 eV

First, we performed relaxation dynamics only on the S_1, S_2, S_6, and S_7 states as a test case both with and without an energy correction to the excited states. The HOMO-LUMO gap for $Au_{38}(SH)_{24}$ is ~ 0.7 eV during the MD simulation, which is ~ 0.15 eV less than the experimental optical gap of ~ 0.9 eV reported elsewhere.[25, 48] Therefore, a 0.15 eV energy correction is added to the excited states to analyze how the relaxation dynamics will differ with the additional energy correction. Adding an energy correction only lengthens the ground state (GS) growth times (by 16-30%) while the decay time constants are less affected. Overall, the time constants and the relaxation trends of these states do not change significantly with the added correction (see SI, Figure S1 and Table S1). Therefore, in this section, the excited state population relaxation dynamics calculations for all twenty-five states (Table 2) will be discussed without the correction

added. The relaxation dynamics of these twenty-five states will provide insights about the core state (~1.5 eV) relaxations in the $Au_{38}(SH)_{24}$ nanocluster.

The GS growth times and decay times were then calculated for states S_1-S_{25} (Table S2). In the presence of all twenty-five states, the population evolutions of the S_1, S_2, S_6, and S_7 states (Figure 5) follow similar relaxation patterns to the case in which only the S_1, S_2, S_6, and S_7 states were considered (Figure S1).

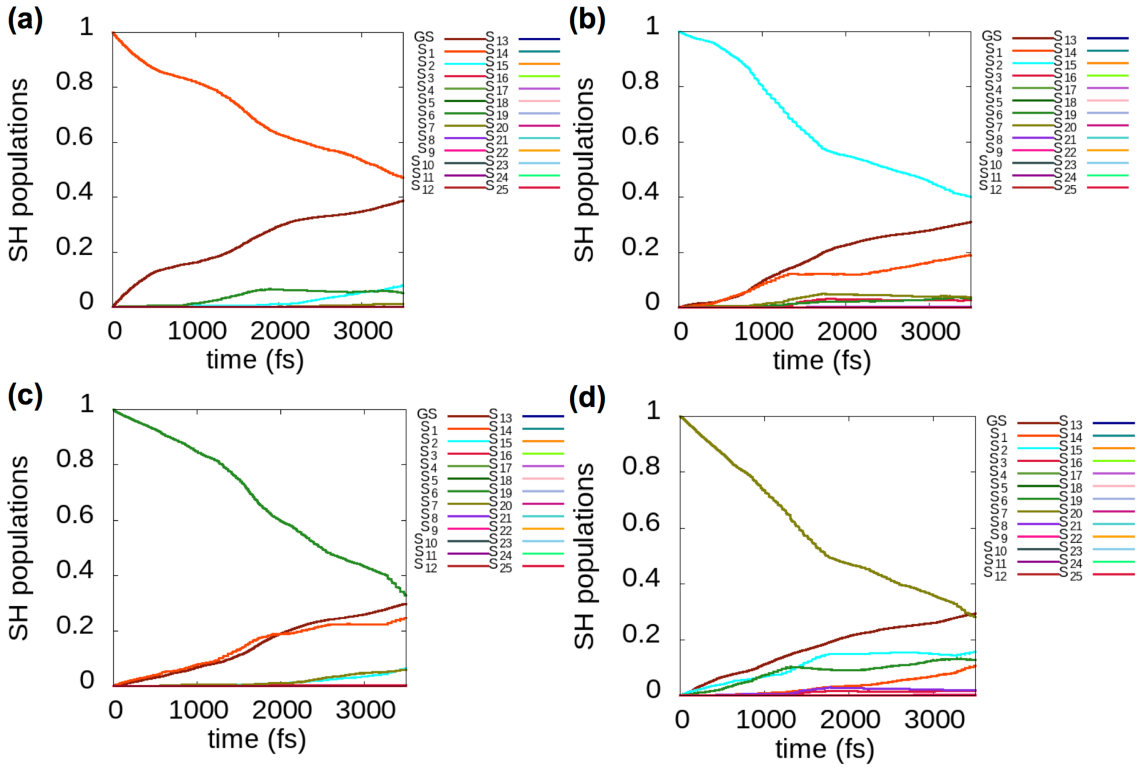

Figure 5. Evolution of excited state populations starting in a) S_1, b) S_2, c) S_6, and d) S_7 excited state.

The GS growth times for the S_1-S_{25} states are in the range of 6.4 – 207 ps. The GS growth times are relatively short except for states S_{15}, S_{19}, S_{20}, S_{24} and S_{25}. The overall growth times are 1-2 orders of magnitude shorter than the growth times of $[Au_{25}(SH)_{18}]^{-1}$,[24] which suggests that the identity of the thiolate-protected nanocluster is a critical factor for tuning the lifetimes of the excited electrons.

The S_{11} state (HOMO-2→LUMO) gives the slowest decay time constant (~ 8.2 ps) when its population is fit to an exponential. However, this S_{11} state population has a non-exponential decay after 2 ps due to population transfer to S_{12} (HOMO-2→LUMO+1)

(Figure 6a). Hops to higher excited states are allowed in the FSSH approach depending on the calculated probability for the hop and whether the kinetic energy of the system is able to accommodate the increase in electronic energy.[38] The S_{12} population mainly transfers back to the S_{11} state (Figure 6b). Due to this reason, fitting the non-exponential S_{11} population decay to an exponential may not result in an accurate decay constant. At 3.5 ps, the S_{11} state retains 57% of its initial excited state population (Figure 6a). Due to fast population exchange between S_{11} and S_{12}, fitting the total population of S_{11} and S_{12} to one exponential could give a better idea about the decay (Figure 6c). The decay constant calculated for the combined S_{11} and S_{12} state population is 9.7 ps. At 3.5 ps, the combined S_{11} and S_{12} states retain 67% of the initial excited state population of S_{11}.

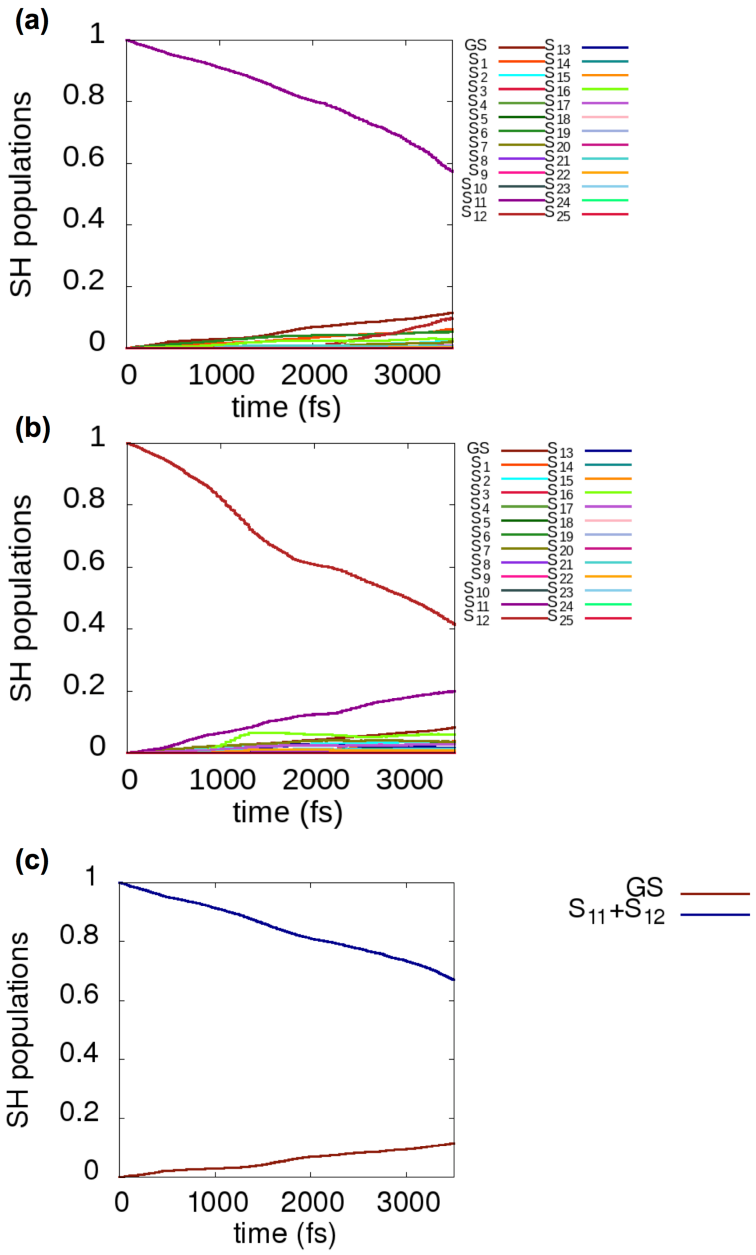

Figure 6. (a) Evolution of excited state populations starting in S_{11}. (b) Evolution of excited state populations starting in S_{12}. (c) Evolution of the total population of the S_{11} and S_{12} states when S_{11} is excited. Populations of other states up to S_{25} are not shown for clarity.

The fitting of the combined population of two or more states to an exponential is expected to be reasonable because several states would be probed by the same pump/probe pulse experimentally, and the observed decay will need to factor in more

than one state. Therefore, we calculated decay time constants for several other combined state populations. At this point, the core states were grouped based on the orbitals involved and possible population transfers between the states. For example, S_1, S_2, S_6 and S_7 originate from the HOMO/HOMO-1 → LUMO/LUMO+1 transitions where the HOMO and HOMO-1 as well as the LUMO and LUMO+1 are nearly degenerate. Thus, the population of S_1 can easily transfer its population to S_2, S_6 and S_7 (Figure 5a). The total population of S_1, S_2, S_6, and S_7 was fit to an exponential when the S_1, S_2, S_6 and S_7 states were excited separately. Similarly, the other cores states were grouped and their combined population decays were calculated (See SI, Table S3). The S_1, S_2, S_6, S_7 total population when the S_6 state was excited and the S_4, S_5, S_9, S_{10} total population when the S_5 and S_{10} states were excited gave slower population decay compared to their individual decay constants. The combined S_1-S_2-S_6-S_7 state population decays are in the range of 6.4-10.1 ps and the combined S_4-S_5-S_9-S_{10} state population decays are in the range of 4.1-10.7 ps. These decay time constants are similar to the combined S_{11}-S_{12} population decay time of 9.7 ps.

At this point it is difficult to compare our decay time constants directly with the experimentally observed time constants. The experimental time constants have been observed by using two pump frequencies (490 nm/1050 nm) and a range of probe frequencies. In our calculations, we look at each state relaxation separately rather than pumping the nanocluster system with a specific frequency. The individual state decay constants calculated for $Au_{38}(SR)_{24}$ in our study are in the range of 2.0–8.2 ps, whereas the combined state population decay constants are in the range of 2.0–10.7 ps. They agree with the picosecond time scale observed experimentally. Our calculations show that the slowest decays (the individual decay of S_{11} or the slowest combined S_{11}-S_{12}, S_1-S_2-S_6-S_7 and S_4-S_5-S_9-S_{10} decays) involve HOMO-2→LUMO/LUMO+1, HOMO/HOMO-1→LUMO/LUMO+1 and HOMO/HOMO-1→LUMO+3/LUMO+4 transitions, which are intracore relaxations (Figure 3).

Relaxation dynamics of the higher excited states up to ~ 2.01 eV

Jin and co-workers have proposed that the faster 1.5 ps decay observed experimentally could arise from a core-shell relaxation or an intracore relaxation in the

lowest energy Au_{38} isomer.[25] They used a probe pulse with the energy covering ~ 0.90-2.33 eV (530 -1300 nm) in their experiments.[25] In this section we analyze the relaxation dynamics of the excited states lying beyond the energy of 1.5 eV in the $Au_{38}(SH)_{24}$ nanocluster optical absorption spectrum (Figure 2). The relaxation dynamics of the excited states lying above 1.50 eV is potentially important in order to understand the involvement of the semiring states, because the 0.00-1.50 eV energy range only covers the gold core states. Here, we have considered the significant excitations appearing in the 0.00-2.01 eV energy range in Figure 2.

There are several notable excitations in the energy range of 1.70-2.01 eV (Table S4). Among them, the excitation around 1.74 eV has a relatively strong oscillator strength value (0.0549) that mainly originates from excitations out of HOMO-6/HOMO-7 orbitals to LUMO/LUMO+1 orbitals (semiring → Π_3) and from the transition out of HOMO-2 to LUMO+2 (Σ_3 → Σ_4). HOMO-6 and HOMO-7 are semiring orbitals whereas HOMO-2 and LUMO+2 are gold core-based orbitals. The transition dipole moment components from the Σ_3 → Σ_4 transition are large even though the weight of this transition is smaller than some of the others. Thus, the 1.74 eV peak is a combination of excitations involving both gold core and semirings where the Σ_3 → Σ_4 transition yields the main contribution due to its high transition dipole moment. The notable excitations around 1.85-2.01 eV have mixed transitions from orbitals involving both gold core and semirings. However, the strongest excitation at 2.01 eV (oscillator strength of 0.1021) is mainly composed from the semiring (HOMO-12/HOMO-13) → LUMO transitions. Comparable findings have been observed by Aikens and co-workers at the PBE/DZ level of theory for $Au_{38}(SR)_{24}$.[28]

Therefore, we considered orbitals ranging from HOMO-13 to LUMO+6 to define the single excitations for the FSSH-TDKS calculations (Table 2, Table S5). The decay times of the excited state population were calculated for all ninety-eight states (Table S6). In the presence of the higher excited states the relaxation trend of the S_1-S_{25} states is preserved. The S_{11} population transfers its population into the S_{12} state although by a lesser amount (Figure S2a). Thus, fitting its population decrease to an exponential may suffer less significant error compared to the case involving only twenty-five states. The S_{12} population primarily transfers back to the S_{11} (Figure S2b). Fitting the S_{11} (HOMO-

2→LUMO) population to an exponential give a slower decay time constant of 7.6 ps. After 3.5 ps, the S_{11} state retains 58% of its initial excited state population (Figure S2a). Fitting the total population of the S_{11} and S_{12} states to an exponential gives a time constant of 8.8 ps. At 3.5 ps, the combined S_{11}-S_{12} state population retains 66% of the initial S_{11} population (Figure S2c). The combined state population decay for the core states were calculated again in the presence of higher states. The S_1, S_2, S_6, S_7 total population when S_6 is excited and the S_4, S_5, S_9, S_{10} total population when S_5 and S_{10} are excited gave slow population decay in the range of 9.7 -10.8 ps, which is similar to the case where only the core states were present.

The higher energy states S_{26}-S_{35} have decay time constants in the range of 1.4 - 4.9 ps. The rest of the higher states (S_{36}-S_{98}) have much shorter time constants in the range of 0.6 - 1.7 ps. The S_{36}-S_{98} states are mainly composed of transitions out of the semiring-based orbitals. In general, the decay times of higher energy states are shorter due to the higher density of states at these energies.

The semiring states mainly arise out of *d* orbitals from gold atoms and *p* orbitals from sulfur atoms. Thus, replacing the H ligands with the experimentally used ligands may not affect excited state energies and their decay times significantly. Slight shifts in energies are possible as different ligands display different electron donating/withdrawing capabilities, although previous work[49, 50] on $Au_{25}(SR)_{18}^-$ has shown that these ligands similarly shift both the HOMO and LUMO and have relatively small effects on excited state energies.

Electron−phonon interactions in the $Au_{38}(SH)_{24}$ cluster

Vibrations in the $Au_{38}(SH)_{24}$ nanocluster can lead to nonradiative relaxation of excited states. Therefore, it is important to understand which nuclear vibrational motions couple most strongly with electronic states to understand the dynamics of electronic relaxations in these systems.

In this section we present the phonon spectral densities obtained for core states (S_1-S_{25}) that demonstrate the vibrational modes that are correlated with the nonradiative relaxations (i.e., relevant electron-phonon interactions). The phonon spectral density plots were obtained by taking Fourier transforms of the normalized autocorrelation function of

the energy gap fluctuation for a pair of electronic excited states of interest. The pair of electronic excited states could be the GS and an electronic excited state or two different electronic excited states. The analysis of the phonon spectral densities showed intense peaks around 24.2, 33.9, 48.4 and 53.2 cm^{-1} for $Au_{38}(SR)_{24}$ when only the core states (up to ~1.5 eV) were considered in the relaxation dynamics (Figure S3). Among the prominent peaks, the peak around 24.4 cm^{-1} was found to be the highest in intensity. This peak at 24.4 cm^{-1} was observed when the spectral densities are plotted considering the energy gap fluctuation between the GS-S_{15}, GS-S_{18}, and GS-S_{23} (Figure 7). The S_{15} excited state arises from the transition out of HOMO-2 to LUMO+4. The S_{18} and S_{23} states arise from the transitions out of HOMO-3 and HOMO-4 to LUMO+2 respectively.

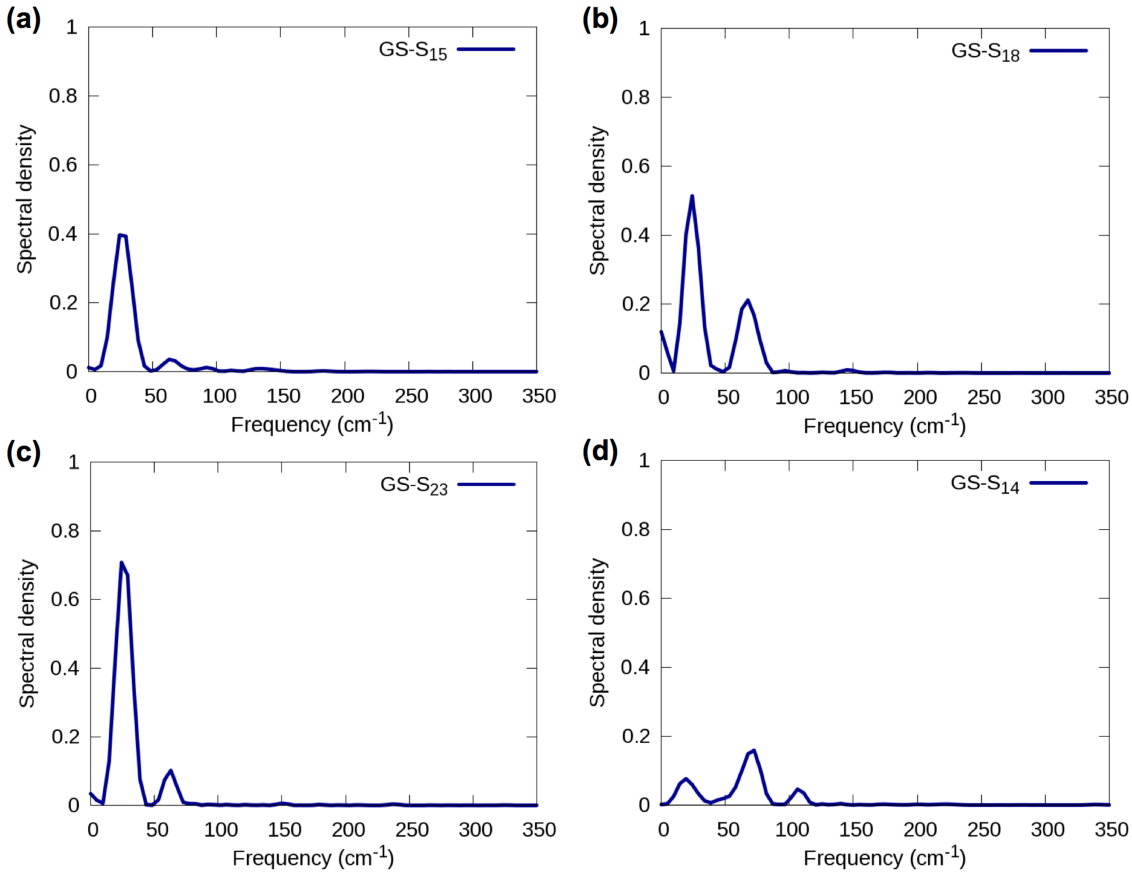

Figure 7. Fourier transforms of autocorrelation functions of the fluctuations of the energy gaps (phonon spectral density spectra) between (a) GS-S_{15} (b) GS-S_{18} (c) GS-S_{23} (d) GS-S_{14}.

To correlate the observed vibrational frequencies to the $Au_{38}(SR)_{24}$ cluster geometry, we compared the phonon modes obtained by the NA-MD calculation to the ground state frequency calculation performed with ADF. The ADF frequency calculation gave several interesting vibrational modes arising from the gold core as well as from semiring motifs. A clear "bending mode" of the bi-icosahedral Au_{23} core at its interior 3-fold face was observed at a very low frequency of 23.5 cm^{-1} and a "fan blade twisting" of two icosahedral units was also observed at 25.9 cm^{-1} (Figure 8). Several other core, semiring and mixed core-semiring vibrational modes were observed in the low frequency range of 27.4 – 43.5 cm^{-1}. Gold core vibrations were noted in the range of 43.5 – 49.2 cm^{-1} including a core breathing mode around 45.1 cm^{-1}. Frequencies in the range of 90.4 – 96.3 cm^{-1} correspond to semiring bending vibrations. Other prominent gold core vibrations are present at a higher frequency of 104.7 cm^{-1} and in the range of 121.1 – 148.3 cm^{-1}. Vibrational modes found in the range of 219.5 – 293.6 cm^{-1} are primarily the Au(core)-S and Au(I)-S stretching modes.

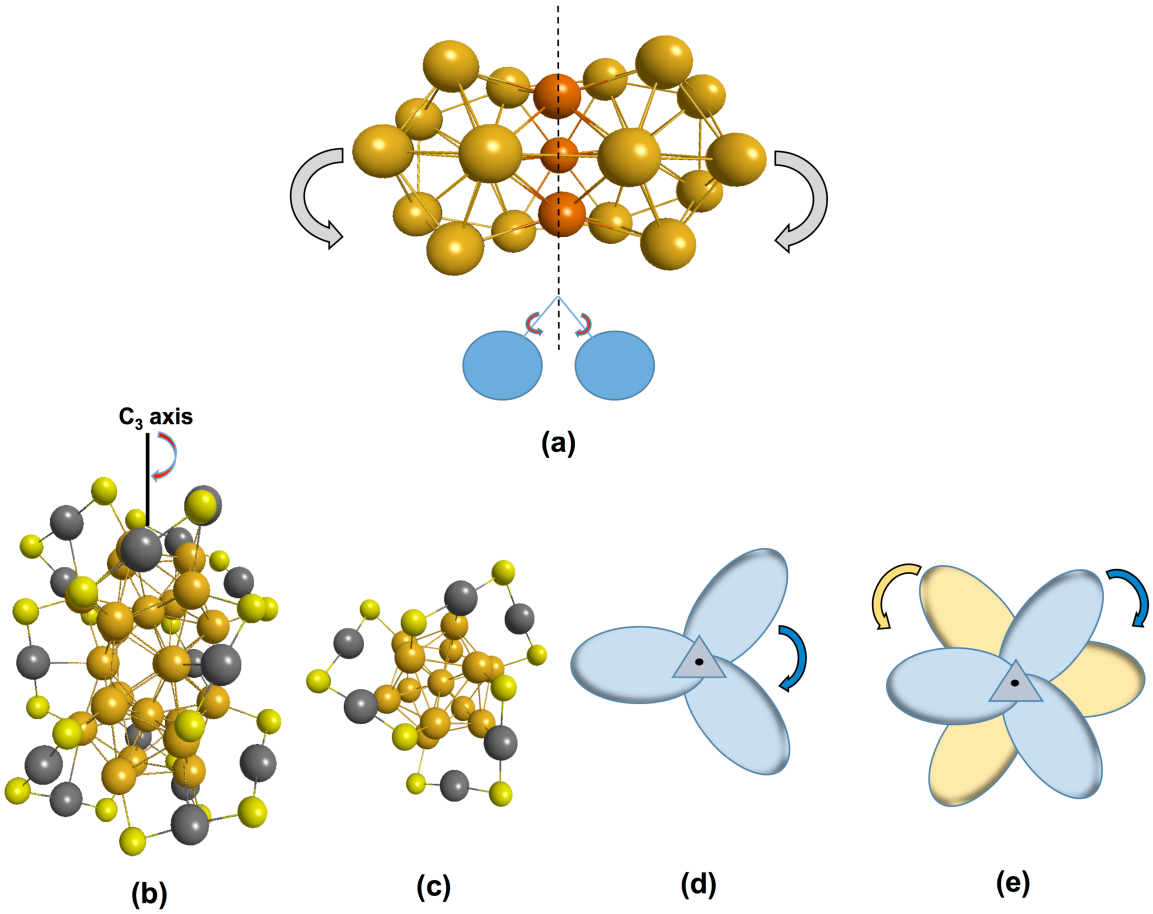

Figure 8. (a) "Bending mode" of the bi-icosahedral Au_{23} core at its interior 3-fold face; (b) side view of the $Au_{38}(SR)_{24}$ cluster, with R ligands not shown; (c) geometric model of three $Au_2(SR)_3$ semirings: top view; (d) fan blade resemblance of the three $Au_2(SR)_3$ semirings (e) "fan blade twisting" mode. (Au-gold, 3-fold face Au-orange, semiring Au-grey, S-yellow)

It is possible that the intense frequency in the phonon spectral density that we observe around 24.4 cm^{-1} from NA-MD calculations is the bending of the bi-icosahedral Au_{23} core or the "fan blade twisting" of two icosahedral units (Figure 8), which could largely lead to nonradiative relaxation of the $Au_{38}(SH)_{24}$ nanocluster. Similarly, the low frequency coherent phonon emission reported at 25 cm^{-1} by Jin and co-workers[25] could also be the bending of the bi-icosahedral Au_{23} core or the "fan blade twisting" mode of two icosahedral units. In addition, there is a very small vibrational mode around 106.5

cm^{-1} in Figure 7d which could be the gold core breathing vibration appearing around 104.7 cm^{-1} in the ADF frequency calculation.

Conclusion

TDDFT and a time-dependent Kohn−Sham description of electron-vibrational dynamics (FSSH-TDKS) have been used to investigate the nonradiative relaxations in the $Au_{38}(SH)_{24}$ nanocluster. The orbital energy variation during the MD simulation indicated a loss of exact degeneracies in orbitals due to geometrical distortions in the cluster during the dynamics. $Au_{38}(SH)_{24}$ has a small HOMO-LUMO gap during the MD simulation which is ~ 0.7 eV. The relaxation dynamics performed on the S_1, S_2, S_6, and S_7 states both with and without an energy correction of 0.15 eV showed that the correction lengthens the GS growth times only by 16-30%.

The GS growth times and excited state decay times were calculated for excited states up to ~ 1.5 eV which covers the Au_{23} core states (S_1-S_{25}). The GS growth times of the S_1-S_{25} states were found to be in the range of 6.4 – 207 ps, which are 1-2 orders of magnitude shorter than the growth times reported for the $[Au_{25}(SH)_{18}]^{-1}$ nanocluster. Relaxation out of the S_{11} state (HOMO-2→LUMO) gives the slowest decay time constant (~ 8.2 ps). Population transfer was observed between S_{11} and S_{12}. Fitting the total population of the S_{11} and S_{12} to an exponential resulted in a decay constant of 9.7 ps. Initial excitations of the S_5, S_6 and S_{10} states gave slow population decay in the range of 9.6 -10.7 ps, which is similar to that for the initially excited S_{11} state. The slowest state decays involve intracore relaxations.

Relaxation dynamics of the higher excited states covering up to ~ 2.01 eV involve relaxations coming from the core, mixed core-semiring, and semiring states (S_1-S_{98}). The relaxation trends of the S_1-S_{25} states were preserved in the presence of all ninety-eight states. Fitting the S_{11} (HOMO-2→LUMO) population to an exponential gave a relatively slow decay time constant of 7.6 ps. Fitting the total population of S_{11} and S_{12} to an exponential gave a time constant of 8.8 ps. The S_5, S_6 and S_{10} excited state decays gave slow time constants in the range of 9.7-10.8 ps. Higher excited states S_{26}-S_{35} have decay time constants in the range of 1.4 - 4.9 ps. The S_{36}-S_{98} states, which consist of transitions out of the semiring orbitals, have shorter time constants in the range of 0.6 -1.7 ps.

Nonradiative relaxation of the $Au_{38}(SH)_{24}$ excited states are driven by nanocluster vibrations. The analysis of the phonon spectral densities showed peaks around 24.2, 33.9, 48.4 and 53.2 cm^{-1} from the NA-MD calculations. The ADF ground state frequency calculation gave several interesting vibrational modes arising from the gold core as well as from semiring motifs. Among them, the low frequency "bending mode" of the bi-icosahedral Au_{23} core at 23.5 cm^{-1} and the "fan blade twisting" mode of two icosahedral units observed at 25.9 cm^{-1} were prominent. One or both of these vibrational modes could be the origin of the low frequency coherent phonon emission experimentally reported at 25 cm^{-1}.

Supporting Information Available

Comparison of excited state lifetimes with and without the energy correction. Ground state population increase lifetimes and excited state population decay lifetimes for the first 25 states and for higher excited states. Transitions involved in the excited states from 1.50-2.01 eV. Fourier transforms of autocorrelations functions of fluctuations of the energy gaps.

Acknowledgments

This material is based on work supported by Department of Energy under grants DE-SC0012273 to CMA and DE-SC0014429 to OVP. The computing for this project was performed on the Beocat Research Cluster at Kansas State University, which is funded in part by NSF grants CHE-1726332, CNS-1006860, EPS-1006860, and EPS-0919443. Beocat Application Scientist Dr. Dave Turner provided valuable technical expertise. The authors are grateful to Prof. Alexey V. Akimov for his support and valuable discussions on PYXAID.

References

1. Herzing, A. A.; Kiely, C. J.; Carley, A. F.; Landon, P.; Hutchings, G. J., Identification of Active Gold Nanoclusters on Iron Oxide Supports for CO Oxidation. *Science* **2008,** *321*, 1331-1335.
2. Yamazoe, S.; Koyasu, K.; Tsukuda, T., Nonscalable Oxidation Catalysis of Gold Clusters. *Acc. Chem. Res.* **2013,** *47*, 816-824.
3. Ide, Y.; Matsuoka, M.; Ogawa, M., Efficient Visible-light-induced Photocatalytic Activity on Gold-Nanoparticle-supported Layered Titanate. *J. Am. Chem. Soc.* **2010,** *132*, 16762-16764.
4. Sarina, S.; Waclawik, E. R.; Zhu, H., Photocatalysis on Supported Gold and Silver Nanoparticles Under Ultraviolet and Visible Light Irradiation. *Green Chem.* **2013,** *15*, 1814-1833.
5. Primo, A.; Corma, A.; García, H., Titania Supported Gold Nanoparticles as Photocatalyst. *Phys. Chem. Chem. Phys.* **2011,** *13*, 886-910.
6. Alvaro, M.; Cojocaru, B.; Ismail, A. A.; Petrea, N.; Ferrer, B.; Harraz, F. A.; Parvulescu, V. I.; Garcia, H., Visible-light Photocatalytic Activity of Gold Nanoparticles Supported on Template-synthesized Mesoporous Titania for the Decontamination of the Chemical Warfare Agent Soman. *Appl. Catal., B: Environmental* **2010,** *99*, 191-197.
7. Yau, S. H.; Varnavski, O.; Goodson III, T., An Ultrafast Look at Au Nanoclusters. *Acc. Chem. Res.* **2013,** *46*, 1506-1516.
8. Qian, H.; Sfeir, M. Y.; Jin, R., Ultrafast Relaxation Dynamics of $[Au_{25}(SR)_{18}]^{q}$ Nanoclusters: Effects of Charge State. *J. Phys. Chem. C* **2010,** *114*, 19935-19940.
9. Sfeir, M. Y.; Qian, H.; Nobusada, K.; Jin, R., Ultrafast Relaxation Dynamics of Rod-shaped 25-atom Gold Nanoclusters. *J. Phys. Chem. C* **2011,** *115*, 6200-6207.
10. Pelton, M.; Tang, Y.; Bakr, O. M.; Stellacci, F., Long-lived Charge-separated States in Ligand-stabilized Silver Clusters. *J. Am. Chem. Soc.* **2012,** *134*, 11856-11859.
11. Mustalahti, S.; Myllyperkiö, P.; Lahtinen, T.; Salorinne, K.; Malola, S.; Koivisto, J.; Häkkinen, H.; Pettersson, M., Ultrafast Electronic Relaxation and Vibrational Cooling Dynamics of $Au_{144}(SC_2H_4Ph)_{60}$ Nanocluster Probed by Transient Mid-IR Spectroscopy. *J. Phys. Chem. C* **2014,** *118*, 18233-18239.
12. Mustalahti, S.; Myllyperkiö, P.; Lahtinen, T.; Malola, S.; Salorinne, K.; Tero, T.-R.; Koivisto, J.; Häkkinen, H.; Pettersson, M., Photodynamics of a Molecular Water-Soluble Nanocluster Identified as Au_{130}(p MBA)$_{50}$. *J. Phys. Chem. C* **2015,** *119*, 20224-20229.
13. Devadas, M. S.; Kwak, K.; Park, J.-W.; Choi, J.-H.; Jun, C.-H.; Sinn, E.; Ramakrishna, G.; Lee, D., Directional Electron Transfer in Chromophore-labeled Quantum-Sized Au_{25} Clusters: Au_{25} as an Electron Donor. *J. Phys. Chem. Lett.* **2010,** *1*, 1497-1503.
14. Jin, R.; Zeng, C.; Zhou, M.; Chen, Y., Atomically Precise Colloidal Metal Nanoclusters and Nanoparticles: Fundamentals and Opportunities. *Chem. Rev.* **2016,** *116*, 10346-10413.
15. Tian, S.; Li, Y.-Z.; Li, M.-B.; Yuan, J.; Yang, J.; Wu, Z.; Jin, R., Structural Isomerism in Gold Nanoparticles Revealed by X-ray Crystallography. *Nat. Commun.* **2015,** *6*, 8667.

16. Zhu, M.; Aikens, C. M.; Hollander, F. J.; Schatz, G. C.; Jin, R., Correlating the Crystal Structure of a Thiol-protected Au_{25} Cluster and Optical Properties. *J. Am. Chem. Soc.* **2008,** *130*, 5883-5885.
17. Zhou, M.; Qian, H.; Sfeir, M. Y.; Nobusada, K.; Jin, R., Effects of Single Atom Doping on the Ultrafast Electron Dynamics of $M_1Au_{24}(SR)_{18}$ (M= Pd, Pt) Nanoclusters. *Nanoscale* **2016,** *8*, 7163-7171.
18. Thanthirige, V. D.; Kim, M.; Choi, W.; Kwak, K.; Lee, D.; Ramakrishna, G., Temperature-Dependent Absorption and Ultrafast Exciton Relaxation Dynamics in $MAu_{24}(SR)_{18}$ Clusters (M= Pt, Hg): Role of the Central Metal Atom. *J. Phys. Chem. C* **2016,** *120*, 23180-23188.
19. Link, S.; El-Sayed, M. A.; Schaaff, T. G.; Whetten, R. L., Transition From Nanoparticle to Molecular Behavior: A Femtosecond Transient Absorption Study of a Size-Selected 28 Atom Gold Cluster. *Chem. Phys. Lett.* **2002,** *356*, 240-246.
20. Miller, S. A.; Womick, J. M.; Parker, J. F.; Murray, R. W.; Moran, A. M., Femtosecond Relaxation Dynamics of $Au_{25}L_{18}^-$ Monolayer-protected Clusters. *J. Phys. Chem. C* **2009,** *113*, 9440-9444.
21. Green, T. D.; Knappenberger, K. L., Relaxation Dynamics of Au_{25} L_{18} Nanoclusters Studied by Femtosecond Time-resolved Near Infrared Transient Absorption Spectroscopy. *Nanoscale* **2012,** *4*, 4111-4118.
22. Stamplecoskie, K. G.; Chen, Y.-S.; Kamat, P. V., Excited-state Behavior of Luminescent Glutathione-Protected Gold Clusters. *J. Phys. Chem. C* **2014,** *118*, 1370-1376.
23. Chen, X.; Prezhdo, O. V.; Ma, Z.; Hou, T.; Guo, Z.; Li, Y., Ab initio Phonon-coupled Nonadiabatic Relaxation Dynamics of $[Au_{25}(SH)_{18}]^-$ Clusters. *Physica Status Solidi (b)* **2016,** *253*, 458-462.
24. Senanayake, R. D.; Akimov, A. V.; Aikens, C. M., Theoretical Investigation of Electron and Nuclear Dynamics in the $[Au_{25}(SH)_{18}]^{-1}$ Thiolate-Protected Gold Nanocluster. *J. Phys. Chem. C* **2016,** *121*, 10653-10662.
25. Zhou, M.; Tian, S.; Zeng, C.; Sfeir, M. Y.; Wu, Z.; Jin, R., Ultrafast Relaxation Dynamics of $Au_{38}(SC_2H_4Ph)_{24}$ Nanoclusters and Effects of Structural Isomerism. *J. Phys. Chem. C* **2017,** *121*, 10686-10693.
26. Green, T. D.; Yi, C.; Zeng, C.; Jin, R.; McGill, S.; Knappenberger Jr, K. L., Temperature-dependent Photoluminescence of Structurally-precise Quantum-Confined $Au_{25}(SC_8H_9)_{18}$ and $Au_{38}(SC_{12}H_{25})_{24}$ Metal Nanoparticles. *J. Phys. Chem. A* **2014,** *118*, 10611-10621.
27. Qian, H.; Eckenhoff, W. T.; Zhu, Y.; Pintauer, T.; Jin, R., Total Structure Determination of Thiolate-protected Au_{38} Nanoparticles. *J. Am. Chem. Soc.* **2010,** *132*, 8280-8281.
28. Lopez-Acevedo, O.; Tsunoyama, H.; Tsukuda, T.; Hakkinen, H.; Aikens, C. M., Chirality and Electronic Structure of the Thiolate-protected Au_{38} Nanocluster. *J. Am. Chem. Soc.* **2010,** *132*, 8210-8218.
29. Pei, Y.; Gao, Y.; Zeng, X. C., Structural Prediction of Thiolate-protected Au_{38}: A Face-fused Bi-icosahedral Au Core. *J. Am. Chem. Soc.* **2008,** *130*, 7830-7832.
30. Knoppe, S.; Bürgi, T., Chirality in Thiolate-protected Gold Clusters. *Acc. Chem. Res.* **2014,** *47*, 1318-1326.

31. Xu, Q.; Kumar, S.; Jin, S.; Qian, H.; Zhu, M.; Jin, R., Chiral 38-Gold-Atom Nanoclusters: Synthesis and Chiroptical Properties. *Small* **2014,** *10*, 1008-1014.
32. Yamazoe, S.; Takano, S.; Kurashige, W.; Yokoyama, T.; Nitta, K.; Negishi, Y.; Tsukuda, T., Hierarchy of Bond Stiffnesses within Icosahedral-based Gold Clusters Protected by Thiolates. *Nat. Commun.* **2016,** *7*, 10414.
33. Negishi, Y.; Igarashi, K.; Munakata, K.; Ohgake, W.; Nobusada, K., Palladium Doping of Magic Gold cluster $Au_{38}(SC_2H_4Ph)_{24}$: Formation of $Pd_2Au_{36}(SC_2H_4\ Ph)_{24}$ with Higher Stability than $Au_{38}(SC_2H_4Ph)_{24}$. *ChemComm* **2012,** *48*, 660-662.
34. Nie, X.; Zeng, C.; Ma, X.; Qian, H.; Ge, Q.; Xu, H.; Jin, R., CeO_2-supported $Au_{38}(SR)_{24}$ Nanocluster Catalyst for CO Oxidation: A Comparison of Ligands-on and -Off Catalysts. *Nanoscale* **2013,** *5*, 5912−5918.
35. Weerawardene, K. D. M.; Guidez, E. B.; Aikens, C. M., Photoluminescence Origin of $Au_{38}(SR)_{24}$ and $Au_{22}(SR)_{18}$ Nanoparticles: A Theoretical Perspective. *J. Phys. Chem. C* **2017,** *121*, 15416-15423.
36. Weerawardene, K. D. M.; Aikens, C. M., Theoretical Insights into the Origin of Photoluminescence of $Au_{25}(SR)_{18}$–Nanoparticles. *J. Am. Chem. Soc.* **2016,** *138*, 11202-11210.
37. Tully, J., Mixed Quantum–classical Dynamics. *Faraday Discuss.* **1998,** *110*, 407-419.
38. Craig, C. F.; Duncan, W. R.; Prezhdo, O. V., Trajectory Surface Hopping in the Time-dependent Kohn-Sham Approach for Electron-nuclear Dynamics. *Phys. Rev. Lett.* **2005,** *95*, 163001.
39. Jaeger, H. M.; Fischer, S.; Prezhdo, O. V., Decoherence-induced Surface Hopping. *J. Chem. Phys.* **2012,** *137*, 22A545.
40. Akimov, A. V.; Prezhdo, O. V., The PYXAID Program for Non-Adiabatic Molecular Dynamics in Condensed Matter Systems. *J. Chem. Theory Comput.* **2013,** *9*, 4959-4972.
41. Akimov, A. V.; Prezhdo, O. V., Advanced Capabilities of the PYXAID Program: Integration Schemes, Decoherence Effects, Multiexcitonic States, and Field-Matter Interaction. *J. Chem. Theory Comput.* **2014,** *10*, 789-804.
42. Perdew, J. P.; Burke, K.; Ernzerhof, M., Generalized Gradient Approximation Made Simple. *Phys. Rev. Lett.* **1996,** *77*, 3865.
43. Te Velde, G. t.; Bickelhaupt, F. M.; Baerends, E. J.; Fonseca Guerra, C.; van Gisbergen, S. J.; Snijders, J. G.; Ziegler, T., Chemistry with ADF. *J. Comput. Chem.* **2001,** *22*, 931-967.
44. Lenthe, E. v.; Baerends, E.-J.; Snijders, J. G., Relativistic Regular Two-Component Hamiltonians. *J. Chem. Phys.* **1993,** *99*, 4597-4610.
45. Kresse, G.; Furthmüller, J., Efficiency of Ab-initio Total Energy Calculations for Metals and Semiconductors using a Plane-wave Basis Set. *Comput. Mater. Sci.* **1996,** *6*, 15-50.
46. Kresse, G.; Joubert, D., From Ultrasoft Pseudopotentials to the Projector Augmented-wave Method. *Phys. Rev. B* **1999,** *59*, 1758.
47. Tsunoyama, H.; Nickut, P.; Negishi, Y.; Al-Shamery, K.; Matsumoto, Y.; Tsukuda, T., Formation of Alkanethiolate-protected Gold Clusters with Unprecedented Core Sizes in the Thiolation of Polymer-stabilized Gold Clusters. *J. Phys. Chem. C* **2007,** *111*, 4153-4158.

48. Qian, H.; Zhu, Y.; Jin, R., Size-focusing Synthesis, Optical and Electrochemical Properties of Monodisperse $Au_{38}(SC_2H_4Ph)_{24}$ Nanoclusters. *ACS Nano* **2009,** *3*, 3795-3803.
49. Aikens, C. M. Geometric and Electronic Structure of $Au_{25}(SPhX)_{18}^-$ (X = H, F, Cl, Br, CH_3, and OCH_3). *J. Phys. Chem. Lett*. **2010**, *1*, 2594-2599.
50. Parker, J. F.; Kacprzak, K. A.; Lopez-Acevedo, O.; Häkkinen, H.; Murray, R. W. Experimental and Density Functional Theory Analysis of Serial Introductions of Electron-Withdrawing Ligands into the Ligand Shell of a Thiolate-Protected Au_{25} Nanoparticle. *J. Phys. Chem. C* **2010**, *114*, 8276-8281.

TOC Graphic

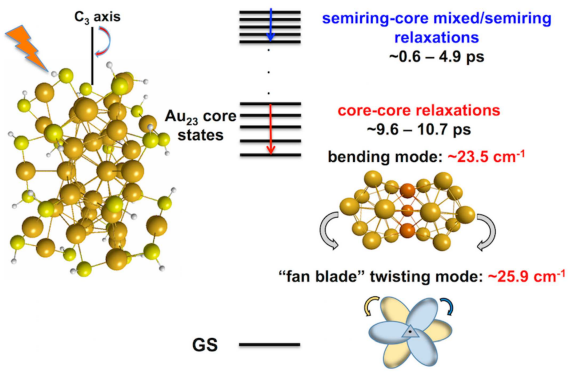
C_3 axis
Au_{23} core states
semiring-core mixed/semiring relaxations
~0.6 – 4.9 ps
core-core relaxations
~9.6 – 10.7 ps
bending mode: ~23.5 cm^{-1}
"fan blade" twisting mode: ~25.9 cm^{-1}
GS